





# Cramer–Rao Lower Bound for SoOp-R-Based Root-Zone Soil Moisture Remote Sensing

Dylan Ray Boyd , *Member, IEEE*, Ali Cafer Gurbuz , *Senior Member, IEEE*, Mehmet Kurum, *Senior Member, IEEE*, James L. Garrison, Benjamin R. Nold, *Graduate Student Member, IEEE*, Jeffrey R. Piepmeier , *Senior Member, IEEE*, Manuel Vega, *Member, IEEE*, and Rajat Bindlish , *Senior Member, IEEE*

**Abstract**—Signals of opportunity (SoOp) reflectometry (SoOp-R) is a maturing field for geophysical remote sensing as evidenced by the growing number of airborne and spaceborne experiments. As this approach receives more attention, it is worth analyzing SoOp-R’s capabilities to retrieve subsurface soil moisture (SM) by leveraging communication and navigation satellite transmitters. In this research, the Cramer–Rao lower bound (CRLB) is used to identify the effects of variable SoOp-R parameters on the best achievable estimation error for root-zone soil moisture (RZSM). This study investigates the use of multiple frequency, polarization, and incidence angle measurement configurations on a two-layered dielectric profile. The results also detail the effects of variable SM conditions on the capability of SoOp-R systems to predict subsurface SM. The most prevalent observation is the importance of using at least two frequencies to limit uncertainties from subsurface SM estimates. If at least two frequencies are used, the CRLB of a profile is retrievable within the root-zone depending on the surface SM content as well as the number of independent measurements of the profile. For a depth of 30 cm, it is observed that a CRLB corresponding to 4% RZSM estimation accuracy is achievable with as few as two dual-frequency-based SoOp-R measurements. For this depth, increasing number of measurements provided by polarization and incidence angle allow for sensing of increasingly wet SM profile structures. This study, overall, details a methodology by which SoOp-R receiver system can be designed to achieve a desired CRLB using a tradeoff study between the available measurements and SM profile.

**Index Terms**—Bistatic, Cramer–Rao lower bound (CRLB), multilayer, reflectometry, root-zone, signals of opportunity (SoOp), soil moisture (SM), specular.

## I. INTRODUCTION

**S**IGNALS of opportunity (SoOp) reflectometry (SoOp-R) within remote sensing refers to the process of leveraging

Manuscript received July 30, 2020; revised September 11, 2020; accepted September 27, 2020. Date of publication October 7, 2020; date of current version October 15, 2020. This work was sponsored by NASA under Grant NNH17ZDA001N-THP and Grant 80NSSC20K1010. (*Corresponding author: Dylan Ray Boyd.*)

Dylan Ray Boyd, Ali Cafer Gurbuz, and Mehmet Kurum are with the Department of Electrical and Computer Engineering, Information Processing and Sensing Lab, Mississippi State University, Mississippi State, MS 39672 USA (e-mail: db1950@msstate.edu; gurbuz@ece.msstate.edu; kurum@ece.msstate.edu).

James L. Garrison and Benjamin R. Nold are with School of Electrical and Computer Engineering, Purdue University, West Lafayette, IN 47907 USA (e-mail: jgarriso@purdue.edu; bnold@purdue.edu).

Jeffrey R. Piepmeier, Manuel Vega, and Rajat Bindlish are with NASA Goddard Spaceflight Center, Greenbelt, MD 20771 USA (e-mail: jeffrey.r.piepmeier@nasa.gov; manuel.vega@nasa.gov; rajat.bindlish@nasa.gov).

Digital Object Identifier 10.1109/JSTARS.2020.3029158

available transmitter sources to perform remote sensing of a geophysical parameter such as ocean surface roughness, sea ice detection, soil moisture (SM), vegetation biomass, or snow water equivalent [1]–[3]. The field has experienced many successful ocean-based applications, experiments, and missions from a dedicated research community since the late 1990s [2], [4]–[6]. This success has since inspired land-based remote sensing applications for SM and snow water equivalent [7]–[13].

One of the most prominent benefits of the SoOp method is its capability to leverage the available frequency sources from noncooperative, anthropogenic transmitters to perform measurements. This is achievable in a cost-efficient manner when compared to traditional radar developments by removing the size, weight, power, and cost (SWaP-C) constraints required for an onboard transmitter. Thus, there is great interest in applying the available frequency sources for ground-based, airborne, and spaceborne applications for remote sensing.

Root-zone soil moisture (RZSM) is a highly sought geophysical observable due to its wide impact across many fields of Earth science such as hydrology, weather forecasting, and crop-yield estimation [14]. RZSM, as the name suggests, is defined as the water content available to a given vegetation’s root-uptake system within a SM profile. Since the root-zone of a given vegetation structure can vary based on root length, the root-zone typically refers to the upper 1 m of a SM profile when discussed irrespective of a particular plant. RZSM data products are a critical resource for hydrological modeling [15].

Within the remote sensing community, remote sensing via radar backscatter is currently the most studied field for determining RZSM. Radar backscatter’s sensitivity to surface SM has been explored as early as the 1970s [16]. This field has advanced to include successful airborne missions using synthetic aperture radar (SAR) based P-band remote sensing systems to provide RZSM products [17], [18]. Studies using radar backscatter at this frequency have detailed the effect of multilayer backscatter for the purpose of RZSM inversion [19].

Recent experiments and simulation studies suggest that multi-frequency observations should be used in resolving RZSM from SoOp-R microwave remote sensing techniques [20]. Some of the most commonly referenced SoOp sources include the Orbcomm communication constellation centered at 137 MHz, the United States Navy’s Ultra-High Frequency Follow-On system centered at 255 MHz and the Mobile User Objective System centered at

370 MHz, Global Navigation Satellite System sources which feature publicly available codes at 1575.42 MHz, and the XM Satellite Radio constellation at 2338 MHz.

While simulations have clearly shown that SoOp-R measurements observe the effects of RZSM when simulating multilayered dielectric structures [20], it is helpful to determine the estimation accuracy of differing SoOp-R configurations on RZSM profiles. Such studies can help design future SoOp-R experiments as well as provide insight on the potential uncertainty embedded within inversion algorithms. To the author's knowledge, no such research has been performed for the use of forward-reflected signals for the purpose of RZSM estimation.

A common technique to compare the performance of any unbiased estimator is the use of the Cramer–Rao lower bound (CRLB) [21]. The CRLB is a popular statistical signal processing technique which expresses a lower bound on the estimation variance providing the best benchmark we can ever expect to achieve with an unbiased estimator. An estimator achieving CRLB is efficient, and it is the minimum variance unbiased estimator for a given model. The CRLB is useful in parameter estimation for remote sensing as it provides a robust metric for characterizing different measurement configurations and its impact on an unknown parameter [22]–[24]. Application of the CRLB to the RZSM problem allows us to determine the estimation bound of any estimator given the same modeling and simulation environment.

This article seeks to determine the estimation accuracy for RZSM for a number of simple SM profile configurations and bistatic SoOp-R scenarios. The simulations consist of many two-slab configurations for RZSM estimation in which the combination of frequencies, incidence angles, and polarizations of signals are considered to achieve the most optimal estimation accuracy possible. The modeling and simulation environment as well as the CRLB calculations are presented in Section II. The simulations are presented in Section III and are discussed in Section IV. Our concluding remarks on the study are presented in Section V.

## II. MODELING AND THEORY

This section presents the theory and modeling for the CRLB study used by this article. Section II-A details the model used to produce the SoOp-R measurements as a function of both ground and system variables. Section II-B presents our implementation of the CRLB for this article. All data presented is simulated.

### A. SoOp-R and Environment Modeling

The model used to simulate the bistatic SoOp-R environment and resulting measurements is the SoOp coherent bistatic scattering model (SCoBi) v1.0.3 [25], [26]. The SCoBi model is a fully polarimetric simulation tool that allows for comprehensive modeling of the ground reflecting surface, geometry, antenna configurations, and cross-channel noise processes. Since the model is based on analytical wave theory, the amplitude and phase information of the coherent signal is preserved through the simulation process. For bare soils, the reflection coefficient is calculated through an iterative process by which the propagation

and reflection processes of a signal incident upon a series of dielectric slabs are calculated directly from Maxwell's equations. The SCoBi model is capable of modeling many features such as multiple SM dielectric representations, vegetation structures, and surface roughness effects.

While the received signals are generally composed of contributions from vegetation, topography, surface roughness, soil type, and water bodies under a typical spaceborne bistatic scenario, we assume a dominantly specular signal over a bare surface SM profile for the purposes of this study. The multi-path reflection coefficient  $\Gamma_{\text{coh}}$  is calculated from the following relation:

$$\Gamma_{\text{coh}} = \underline{g}_{\underline{r}}(\hat{o}_s^+) \cdot \underline{u}_{s \rightarrow r}(\hat{o}_s^+) \cdot \underline{r}_s(\hat{o}_s^+, \hat{i}_s^-) \cdot \underline{u}_{t \rightarrow s}(\hat{i}_s^-) \cdot \underline{g}_t(\hat{i}_s^-) \cdot \underline{e}_t \quad (1)$$

where  $i$  and  $o$  describe the incoming and outgoing directions of the wave propagation,  $\underline{g}_{\underline{r}}$  and  $\underline{g}_{\underline{t}}$  are the receiver gain and transmitter gain, respectively,  $\underline{u}_{s \rightarrow r}$  and  $\underline{u}_{t \rightarrow s}$  represent the polarization basis transformation between specular-point-to-receiver and transmitter-to-specular-point, respectively,  $\underline{r}_s$  is the specular reflection matrix, and  $\underline{e}_t$  is the nominal polarization state. More details on the derivation of the reflection coefficient and its constituent parameters can be found in [25].

This problem assumes specular-dominant contributions based on the system geometry and previous research findings [27]. For this study, we assume a fixed altitude and azimuth. Because of the flat homogeneous slabs that are used in this study, many parameters will have negligible effect on the received signal. Under a specular reflection assumption where the surface roughness is within the Rayleigh scattering regime, the contributing area of the spatial footprint is restricted to the first Fresnel zone [3], which varies as a function of frequency, incidence angle, and platform altitude. However, because the reflecting surface is assumed to be semi-infinite and homogeneous within each layer, factors such as spatial resolution and azimuth direction can be ignored.

A simplified depiction of the modeling and simulation environment for this article's simulations is shown in Fig. 1. The receiver is pointed directly toward the specular point, and no antenna losses are simulated. The primary system variables considered are transmitter frequency, transmitter incidence angle (equal to the surface scattering angle for bare soils), and receiver polarization. While some communication satellite systems use left-hand circular polarization (L), all transmitter polarizations in this study are fixed at right-hand circular polarization (R) in order to more easily describe the copolarization and cross-polarization relationships with the CRLB.

For simplicity and ease of understanding, the SM profile is represented by two layers: 1) a surface SM value extending from the air–surface interface to the next dielectric discontinuity, and 2) a second slab extending downward infinitely across the half-space. The dielectric value of these two slabs is calculated using the Mironov dielectric model [28]. This model is parameterized by volumetric SM (VSM) and soil clay content. The

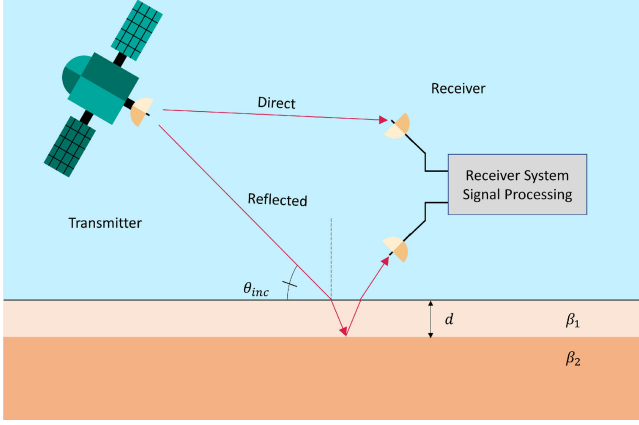


Fig. 1. Simplified geometry of this article’s modeling and simulation environment. The unknown SM variables are designated as  $\beta_1$  and  $\beta_2$  for the first and second SM slabs. No surface roughness is assumed. An initial slab is assumed to contain constant SM from the surface until the dielectric discontinuity at location  $d$ . The SM content ( $\beta_2$ ) at depth  $d$  is considered to be the root-zone for this study.

latter of which is assumed to be 31% for this study. As previously mentioned, surface roughness is not considered.

The general geometry in this simulation study, while capable of being modeled in SCoBi, is simplified to constant values. SCoBi is capable of modeling antenna beam patterns as well as losses from polarization mismatch and antenna cross-talk. However, full consideration of the bistatic geometry between the transmitter, receiver, and specular point should be considered when implementing such an analysis. Since such a study would require fixed points of reference relative to the location of transmitters, antenna beam direction (including both incidence and azimuth angle), and the physical location of the receiver, we choose to assume these values are negligible so that the results are generalized for SoOp-R applications.

Soil texture is an important parameter in establishing the dielectric of soil because soil texture can change the distribution of water content within a soil layer. Clay content, the configurable parameter for the Mironov soil dielectric model, changes the dielectric of soil nonlinearly. However, because soil texture does not change significantly over time like SM, it is common to assume that it is static as we do in this study.

### B. Cramer–Rao Lower Bound Model

The CRLB is considered to be one of the simplest methods for placing a lower bound on the variance of any unbiased estimator. It also provides a way for determining the minimum variance unbiased estimator. In the case of a deterministic modeling and simulation scenario, the CRLB presents the ultimate performance of an unknown parameter estimator for the given set of specific model inputs. Although CRLB defines the performance bound, the maximum likelihood estimator is an asymptotically efficient attaining CRLB.

Since all of our information about estimating the RZSM parameter is embodied in the observed measurements and the underlying probability distribution function (PDF) for that data,

the CRLB that defines the estimation accuracy also depends on the PDF. We use the SCoBi model to simulate the coherent reflection coefficient measurements.

We first discuss the parameterization of our forward model and simulation environment for the CRLB calculation. After having fixed certain parameters within the SCoBi model, the remaining controllable variables are described. The controllable parameters will be contained in the vector  $\mathbf{x} = [f, \theta_{inc}, q]$  where  $f$  is the frequency of the transmitter and receiver,  $\theta_{inc}$  is the incidence angle of the signal at the air–surface boundary, and  $q$  is the polarization of the receiver antenna. The unknown parameter vector representing the SM of the upper and lower layers is given by  $\beta = [\beta_1, \beta_2]$ . The output reflection coefficient  $\Gamma_{coh}$  from (1) is computed using the forward SCoBi model  $f_{SCoBi}(\mathbf{x}; \beta)$ . The output measurement  $y$  is the sum of our model output and measurement noise  $n$

$$y = f_{SCoBi}(\mathbf{x}; \beta) + n. \quad (2)$$

The measurement noise in (2) is assumed to be a zero-mean white Gaussian process for the reflection coefficient with a common variance of  $\sigma^2$ . As the reflection coefficient is a complex number, the noise power is assumed to be distributed evenly across the real and imaginary components of the signal. Selecting a noise term for the reflection coefficient should adequately reflect typical noise values observed by SoOp-R systems.

The SCoBi model output buried in Gaussian noise is treated as a multivariate PDF whose inputs are defined by the measurement vector  $\mathbf{y}$ , system input vector  $\mathbf{x}$ , and unknown parameter vector  $\beta$  as defined in the following equation:

$$p(\mathbf{y}; \mathbf{x}, \beta) = \mathcal{N}(f_{SCoBi}(\mathbf{x}, \beta), \sigma^2 \mathbf{I}). \quad (3)$$

Under these conditions, the CRLB for parameter  $\beta_i$  is found as the  $[i, i]$ th element of the inverse of a matrix

$$\text{var}(\hat{\beta}) \geq [\mathbf{F}^{-1}(\beta)]_{ii} = \text{CRLB}(\beta_i) \quad (4)$$

where  $\mathbf{F}(\beta)$  is the  $\alpha \times \alpha$  Fisher information matrix that is defined by

$$[\mathbf{F}(\beta)]_{ij} = -E \left[ \frac{\partial^2 \ln p(\mathbf{x}; \beta)}{\partial \beta_i \partial \beta_j} \right] \quad (5)$$

for  $i, j = 1, 2, \dots, \alpha$ , where  $\alpha$  is the total number of unknown parameters [21]. In our case, representing the unknown RZSM with  $\beta = [\beta_1, \beta_2]$  for upper and lower layers,  $\alpha = 2$  and the matrix  $\mathbf{F}(\beta)$  is  $2 \times 2$ . However, the presented CRLB model is able to handle any given number of unknown parameter settings.

In addition, since our model is a complex multivariate Gaussian [29], [30], calculation of the Fisher information matrix can further be simplified using

$$\mathbf{F}_{ij} = \frac{2}{\sigma^2} \Re \left( \left[ \frac{\partial f_{SCoBi}(\mathbf{x}, \beta)}{\partial \beta_i} \right]^H \left[ \frac{\partial f_{SCoBi}(\mathbf{x}, \beta)}{\partial \beta_j} \right] \right). \quad (6)$$

### III. SIMULATION STUDY

The following study presents multiple simulations which examine the resultant CRLB when the input for the modeling and simulation environment is changed. Specifically, the five

main variables of interest are frequency, incidence angle, polarization, SM content, and SM slab position. As some simulations require slightly different environments to illustrate the effect of certain inputs, the methodology for each simulation is presented alongside the associated results. Working under the assumption that the square root of the lower bound is directly comparable to SM retrieval accuracy constraints, all results will depict the  $\sqrt{\text{CRLB}}$ . For all figures depicting the  $\sqrt{\text{CRLB}}$  along the  $y$ -axis, each subplot shows the value as a percentage instead of natural units.

All simulations share certain common features. The  $\sqrt{\text{CRLB}}$  is calculated using measurements from the combination of all available inputs (e.g., a simulation at 3 frequencies, 2 angles, and 2 polarizations will produce 12 measurements to determine the  $\sqrt{\text{CRLB}}$ ). All measurements use a common noise variance  $\sigma^2$  based on a reflectivity noise floor of  $-34$  dB. This value is chosen based on the distribution of 2017 and 2018 CYGNSS reflectivity observations over land [31]. While it is likely that different communication systems will observe different noise distributions, a common noise variance for all frequencies will help focus the simulations on a generalized characterization of the impact of the receiver system variables. Nearly all measurements are performed using a SM profile consisting of two slabs where the first slab extends from the air–surface interface to a depth  $d$  in centimeters. When the five commonly available SoOp-R transmitters at 137.5, 255, 370, 1575.42, and 2338 MHz are used as variable parameters in subsequent figures, these frequencies are denoted as  $a, b, c, d,$  and  $e$  in order to achieve efficient spacing within the figures.

The following study intends to show the reader the benefits of using different combinations of frequencies, polarizations, and incidence angles for different SM values and RZSM depth positions. Similar to the concept of dropout in neural network regularization, this study begins with a large number of measurements and removes parameters that are unnecessary to obtain the desired RZSM retrieval estimation accuracy. The number of parameters used is larger than what can be expected from most experimental applications. However, by visualizing “smooth”  $\sqrt{\text{CRLB}}$  gradients from the use of a large number of measurements, it is our intention to more easily visualize the influences of frequency, polarization, and incidence angle to the reader by removing these parameters and observing their impact on the  $\sqrt{\text{CRLB}}$  calculation.

#### A. CRLB as Function of Depth and Frequency

In this section, the relationship between the  $\sqrt{\text{CRLB}}$ , frequency, and sensing depth is examined. In the context of this article, the sensing depth refers to positions within the root-zone where the second slabs SM content ( $\beta_2$ ) can be sensed within a desired degree of error. A target  $\sqrt{\text{CRLB}}$  that is less than or equal to 4% will be the primary focus since this is a commonly targeted goal for surface SM estimation.

While penetration depth is a good metric for establishing a general depth where signal contributions can be sensed, the most commonly used penetration depth formula assumes a single SM value for the entire profile and, therefore, cannot account for the

reflection properties of multilayer dielectric structures. For this reason, the  $\sqrt{\text{CRLB}}$  will be used directly to determine depths where RZSM can be sensed with a desired 4% accuracy.

To establish a reasonable depth for RZSM estimation with this article’s system configuration, two initial cases are presented. First, a scenario where 120 SoOp-R measurements are used to determine the  $\sqrt{\text{CRLB}}$ . For the second scenario, we then restrict the measurements to only five values. These two simulations are used to illustrate the range of potential RZSM depths  $d$  where a  $\sqrt{\text{CRLB}}$  estimation accuracy of 4% can be achieved. While it is unlikely to obtain 120 measurements over short temporal spans in field applications, this initial number of parameters allows us to visualize the  $\sqrt{\text{CRLB}}$  while mitigating anomalies that stem from an undesirable combination of measurements.

The  $\sqrt{\text{CRLB}}$  is calculated across the upper 1 m of an example SM profile. For a two-slab profile, the second slab is lowered within the profile to examine the effects that the location of the second slab (i.e., the RZSM slab) induce on the  $\sqrt{\text{CRLB}}$ . Because there are only two layers, this can also be described as moving the position of the single dielectric discontinuity within the profile deeper into the soil. Two configurations are used in this study. One configuration assumes 120 reflection coefficient measurements from the combination of values resulting from the five frequencies, six incidence angles equally spaced from  $20^\circ$  to  $70^\circ$ , and the four receiver polarizations ( $X, Y, L,$  and  $R$ ). The second configuration assumes five measurements collected at the five available frequencies with each measurement occurring at  $L$ -polarization and a  $20^\circ$  incidence angle.

Fig. 2 presents the resultant  $\sqrt{\text{CRLB}}$  values for the RZSM ( $\beta_2$ ) estimates. The  $x$ -axis indicates the location of the dielectric discontinuity within the profile. Each subplot within the figure indicates the SM content of the second slab (i.e., RZSM), while the different colored lines represent the SM value of the first slab (i.e., surface SM). The upper-left and upper-right subplots within the figure indicate the first measurement configuration using 120 measurements, while the lower-left and lower-right subplots indicate the second measurement configuration of only five measurements.

It is immediately apparent that the depth for resolving RZSM  $\beta_2$  is dependent on the SM profile and receiver configuration. An important factor for this behavior is the nature of subsurface reflection properties which are dominantly controlled by the dielectric contrast of subsurface slabs [20]. As the size of the surface SM slab increases, the waves propagating through the first slab will undergo more attenuation processes which make RZSM retrieval more difficult. If we observe an RZSM value of 20%, we find that the point at which our RZSM estimation reaches  $\pm 4\%$  accuracy is at 71, 45, 30, and 24 cm for surface SM values of 20% , 30% , 40% , and 50% VSM. Given five measurements, this same estimation accuracy is achieved at depths of 41, 27, 20, and 15 cm for the same SM and RZSM values. This simulation, therefore, shows the potential variable depths at which we can estimate RZSM for a specified accuracy range of  $\pm 4\%$ .

The  $\sqrt{\text{CRLB}}$  for surface SM estimates  $\beta_1$  were also calculated alongside each value for  $\beta_2$ , although they are not depicted. The surface SM estimates show that the surface SM  $\sqrt{\text{CRLB}}$

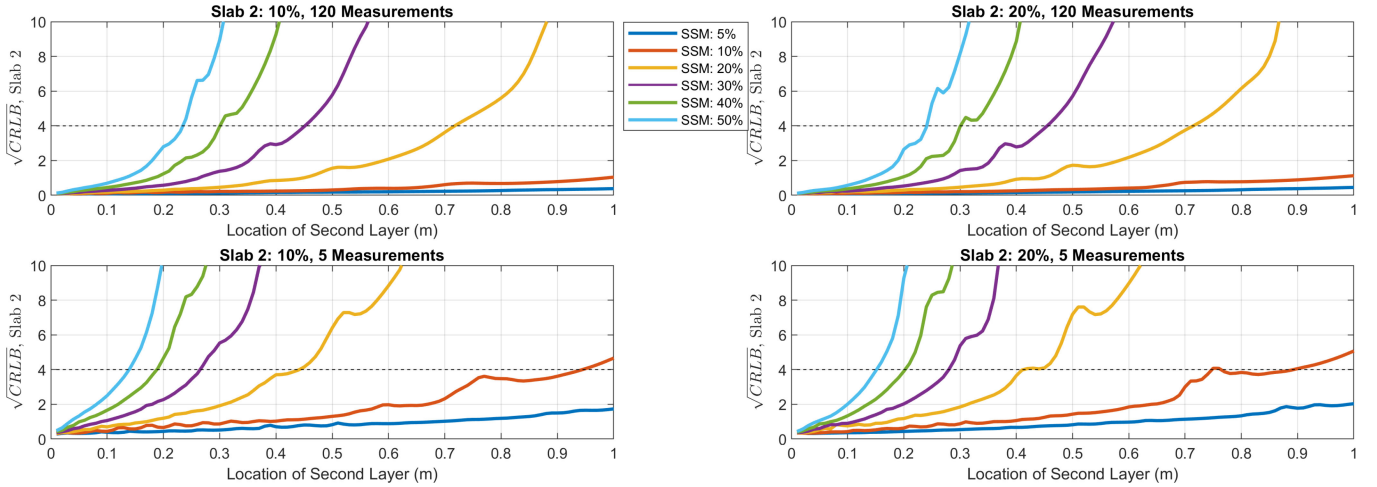


Fig. 2. Root-zone soil moisture  $\sqrt{\text{CRLB}}$  as a function of depth. The upper two subplots show the  $\sqrt{\text{CRLB}}$  from the combination of five frequencies (137, 255, 370, 1575.42, and 2338 MHz), six angles ( $20^\circ$ ,  $30^\circ$ ,  $40^\circ$ ,  $50^\circ$ ,  $60^\circ$ , and  $70^\circ$ ), and four polarizations ( $X$ ,  $Y$ ,  $L$ , and  $R$ ) producing 120 measurements. The bottom two subplots show five measurements from 137, 255, 370, 1575.42, and 2338 MHz at  $L$ -polarization and  $20^\circ$  incidence.

is always lower-bounded significantly lower than the desired accuracy range of  $\pm 4\%$  as expected. When changing from 120 measurements to 5 measurements, the worst-case CRLB changes from less than 0.4% to roughly 1%. Thus, the multi-frequency measurements are capable of resolving the surface SM regardless of the SM content or location of the dielectric discontinuity within these simulations.

Having established the effect that depth has on the  $\sqrt{\text{CRLB}}$  when five frequencies are used for many SM profiles, we now examine the effect of frequency combinations and RZSM depth simultaneously. Fig. 3 depicts the resultant  $\sqrt{\text{CRLB}}$  for these simulations for the RZSM ( $\beta_2$ ). The results are restricted to example SM profiles featuring relatively high SM content. The frequencies used are 137, 255, 370, 1575, and 2338 MHz which are represented by the letters  $a$ ,  $b$ ,  $c$ ,  $d$ , and  $e$  along the  $x$ -axis of each subplot. The depth of the slab position is indicated along the  $y$ -axis. Within the simulation, the slab is moved in 1-cm increments down the SM profile. The upper-left and upper-right subplots feature a surface SM of 20% and an RZSM value of 10% and 30%, respectively. The lower-left and lower-right subplots feature a surface SM of 30% and an RZSM value of 20% and 40%, respectively. This is performed to visualize a consistent dielectric contrast with respect to SM value for each row of subplots. While this article is interested in understanding depths where a 4% estimation error can reliably be obtained, the results are thresholded up to a maximum  $\sqrt{\text{CRLB}}$  of 10% to provide understanding of the increasing estimation error with respect to depth, frequency combinations, and SM profile structure.

The results of Fig. 3 show distinct changes with respect to SM content as well as the number of frequencies used. The visually striking group of pixels which exceed the  $\sqrt{\text{CRLB}}$  threshold of 10% in this image are observed at frequencies of 1575 and 2338 MHz ( $d$  and  $e$ ). Due to the shorter wavelengths, these signals show limited configurations where RZSM can be sensed. For example, in the upper-right subplot of Fig. 3, the  $\sqrt{\text{CRLB}}$  derived exclusively from 1575 MHz reaches high error

values around 22 cm, and the 2338 MHz signal reaches high error values around 12 cm. By lowering the RZSM slab further into the profile, contributions from these depths are buried in noise.

Across the range of frequency combinations along the  $x$ -axis, the  $\sqrt{\text{CRLB}}$  for measurements using a surface SM value of 20% remain far below the 10% threshold up to the  $y$ -axis limit of 45 cm for most dual-frequency combinations. Whenever the surface SM is increased to 30%, only portions of the dual-frequency combinations can sense below the maximum  $\sqrt{\text{CRLB}}$  threshold, and the RZSM value can be seen to alter the depth where this threshold is reached for frequency combinations. This threshold indicates an area where the signal becomes buried by our system noise and can no longer be confidently used in RZSM estimation. As visualized in the lower-left subplot, the use of multiple frequencies can allow for RZSM estimation deeper into the profile than the maximum depth of a single frequency's estimation capabilities.

There are multiple depths where the RZSM can be estimated using a single frequency when the SoOp-R signal remains above the noise floor. As mentioned previously, this is caused by frequency and depth-dependent properties of the signals interaction with the profile. While this indicates that an estimator which can achieve a desirable  $\sqrt{\text{CRLB}}$  from a single frequency might exist, this estimator is likely insufficient for handling changes in the SM gradient.

Throughout Fig. 3, there are many instances of abrupt changes in  $\sqrt{\text{CRLB}}$  along different depths. For example, a sharp increase in  $\sqrt{\text{CRLB}}$  occurs at 33 cm for 137 MHz ( $a$ ) and at 30 cm for 255 MHz ( $b$ ) in the upper-left subplot. This occurs for two reasons. When the Jacobian matrix is calculated with respect to the unknown SM parameters, certain depths will exhibit limited change with respect to SM. Because of the coherency of the reflection coefficient, we note that this generally occurs at a point where the reflection coefficient has reached a maximum or minimum with respect to depth. Thus, there are depths where

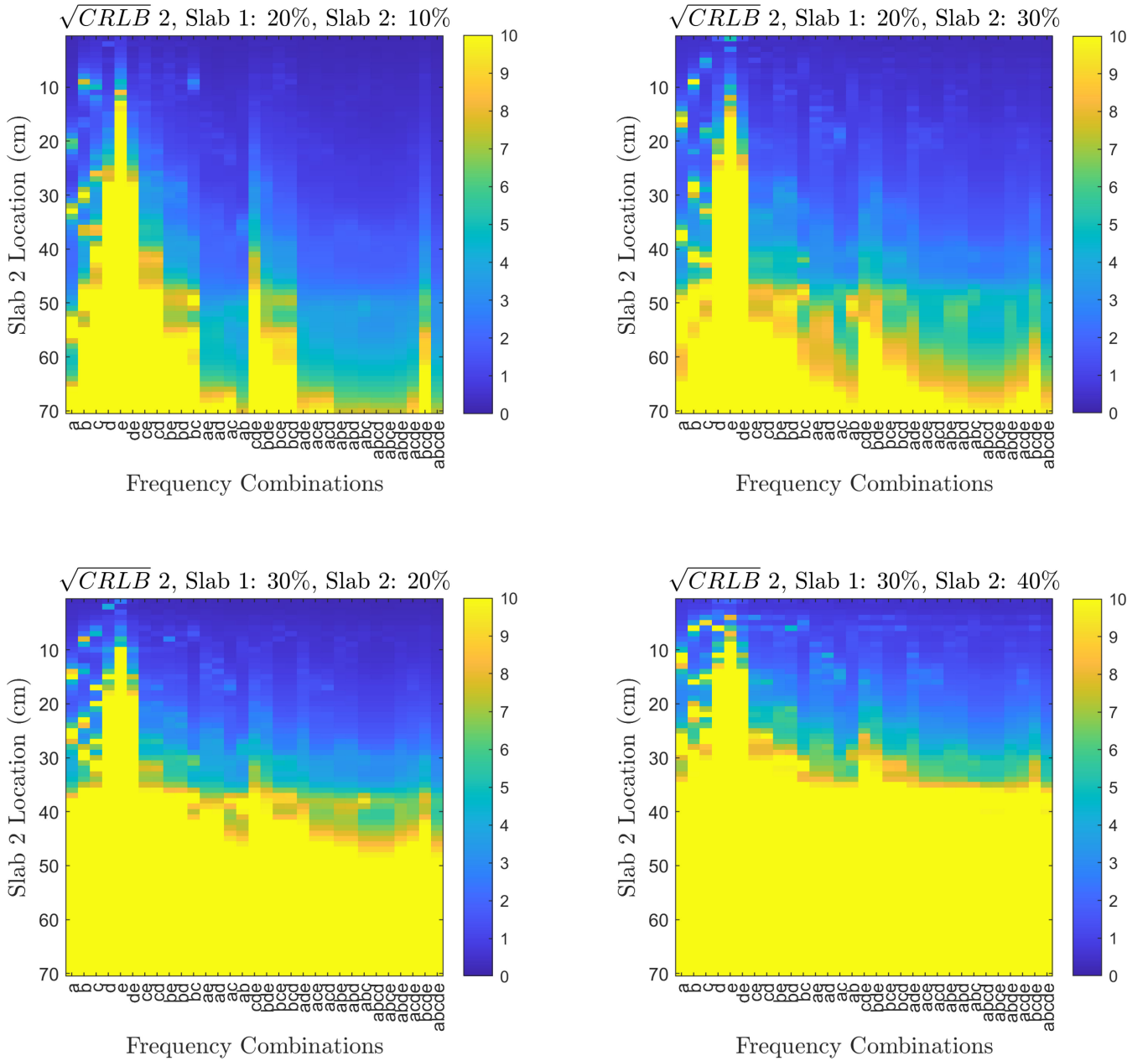


Fig. 3.  $\sqrt{\text{CRLB}}$  of RZSM as a function of depth and frequency for wet SM profiles. Frequency combinations are noted along the  $x$ -axis where  $a$ ,  $b$ ,  $c$ ,  $d$ , and  $e$  correspond to 137, 255, 370, 1575, and 2338 MHz, respectively. Each frequency samples measurements in  $X$  and  $Y$  polarization as well as at  $20^\circ$ ,  $45^\circ$ , and  $70^\circ$  incidence. The location of the second slab is shown on the  $y$ -axis, and the value of the resultant  $\sqrt{\text{CRLB}}$  is shown by the color bar.

perturbing the forward model with respect to SM will observe limited change due to the frequency-dependent coherency fluctuations of the reflection coefficient. The resulting matrix multiplication and inversion of the Fisher-information matrix based on these points of insensitivity to perturbation generate the large  $\sqrt{\text{CRLB}}$  values seen. Because these points are dependent on the SM profile layering, frequency, and SM content, it is difficult to know where these insensitive points will appear prior to measurements. For this reason, we suggest the leveraging of multiple frequencies to make efficient use of these coherency effects.

It is evident from these simulations that longer wavelengths are generally better estimators than shorter wavelengths. The use of the lowest frequency (137 MHz,  $a$ ) generally provides the deepest estimation levels as shown in the upper-left subplot. When combined with another frequency, most  $\sqrt{\text{CRLB}}$  fluctuations are eliminated. For estimation of RZSM, the combination of the three lowest frequencies ( $abc$ ) tends to provide the deepest estimation. The inclusion of the two higher frequencies ( $abcde$ ) is seen to eliminate most large fluctuations in  $\sqrt{\text{CRLB}}$  across all depths. Thus, for deeper RZSM estimation, the use of 137 MHz is suggested.

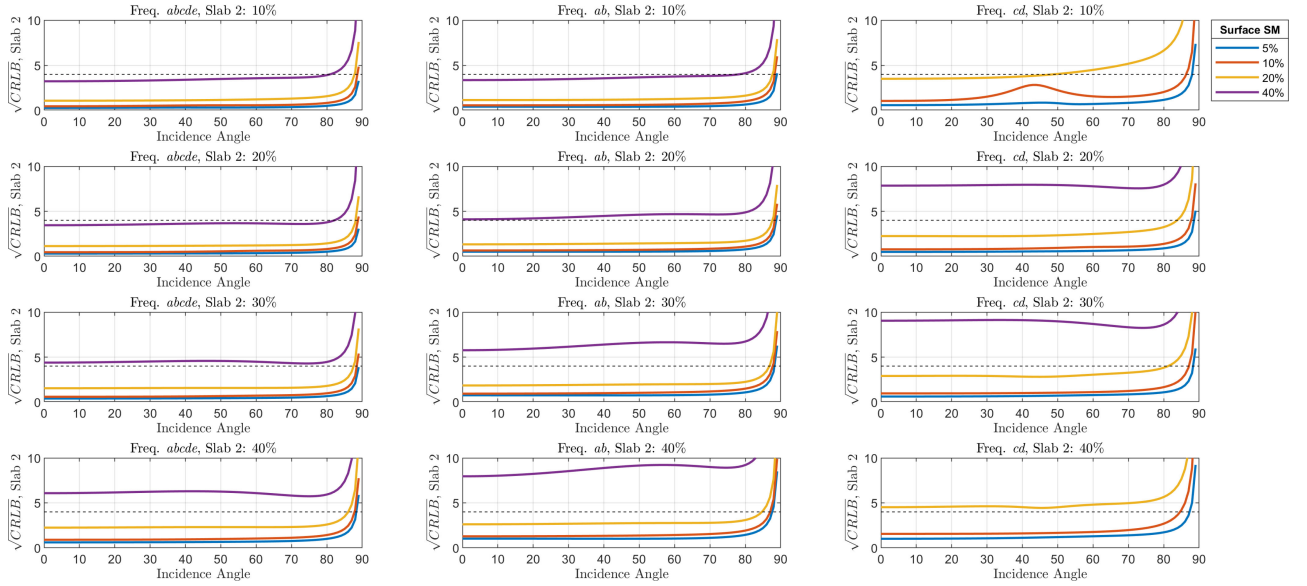


Fig. 4. Root-zone soil moisture  $\sqrt{\text{CRLB}}$  as a function of incidence angle. Each column represents a combination of frequency values where the combinations are (137, 255, 370, 1575.42 and 2338.75 MHz), (137 and 255 MHz), and (370 and 1575.42 MHz.) Each frequency value is indicated by the letters *a*, *b*, *c*, *d*, and *e* in ascending order. Each measurement uses *X* and *Y* polarizations. Each row indicates the value of the SM in the second slab, and the color of each line shows the SM in the first slab.

Similar to the previous simulation, the surface SM's  $\sqrt{\text{CRLB}}$  was calculated for each frequency and depth combination shown in Fig. 3. The calculations, in most cases, resulted in estimation error far below 0.5%. However, it should be noted that shorter wavelengths (*L*-band or higher) performed more consistently at estimating surface SM as longer wavelengths are generally more sensitive to variations in subsurface SM.

In summary, the use of multiple frequencies for estimating *RZSM* is important for repeatable, accurate estimation of  $\sqrt{\text{CRLB}}$  with longer wavelengths proving to be the most useful for estimation at deeper points in the profile. From a physics-based perspective, it is known that the use of a single frequency can result in ambiguity with respect to depth contributions due to propagation effects and the sinusoidal oscillations of reflection coefficient values as a function of depth. By using multiple frequencies, there is a higher probability of observing depth-dependent signal interactions within the profile, enabling better and more consistent estimation. In the following simulations, the combination of the two lowest frequencies (137 and 255 MHz) as well as combinations of a low and higher frequency (370 and 1575 MHz) are depicted to further illustrate the impact of frequency-specific combinations on estimation accuracy.

### B. CRLB as a Function of Variable and Configurable System Parameters

Within this section, we observe the impact of incidence angles and polarization on  $\sqrt{\text{CRLB}}$ . Based on the previous results, a fixed depth of 30 cm is chosen **color red** for all subsequent analyses as this location shows good estimation accuracy despite increased SM content and reduced frequency observations. For each simulation, we observe the impact that combinations of

polarization and incidence angle have on the resultant  $\sqrt{\text{CRLB}}$  while the remaining parameters are fixed.

1) *Varying Angle*: The effect of using different incidence angles on the  $\sqrt{\text{CRLB}}$  is visualized in Fig. 4. Each measurement uses two polarizations (*X* and *Y*) and a combination of frequencies to calculate the  $\sqrt{\text{CRLB}}$ . The left-most column depicts the combination of all five frequencies, the middle column depicts the combination of 137 and 255 MHz, and the right column depicts the combination of 370 and 1575.42 MHz. Each row represents a different SM value for the second dielectric slab.

The general shape of the  $\sqrt{\text{CRLB}}$  value across the incidence angle sweep is worth discussing from this figure. When all five frequencies are used, no angle performs better than another if the simulation stays away from the grazing angle. However, as we go beyond 75°, the performance of the estimation begins to degrade dramatically. This is in agreement with many spaceborne radar quality control filtering processes to limit measurements near 65°. For the simulations in this study, it is suggested that angles below 75° can be used with relatively equal and positive impact for estimating *RZSM*.

The middle and right columns separate the problem into two groups of dual frequency combinations. As demonstrated earlier, it is more difficult to estimate moist soils (especially at 30% or above) given reduced frequency measurements. However, the use of the two lowest available frequency values provides the most optimal estimation for the fewest visualized parameters. In contrast to the  $\sqrt{\text{CRLB}}$  values using five frequencies, the values using two frequency measurements feature larger fluctuations in the  $\sqrt{\text{CRLB}}$  at different surface SM values and at different incidence angles. This is explained by the shifting insensitivity of certain frequencies to a given SM profile configuration which impact the  $\sqrt{\text{CRLB}}$ . When more frequency observations are added, the abrupt changes in  $\sqrt{\text{CRLB}}$  seen in the dashed line

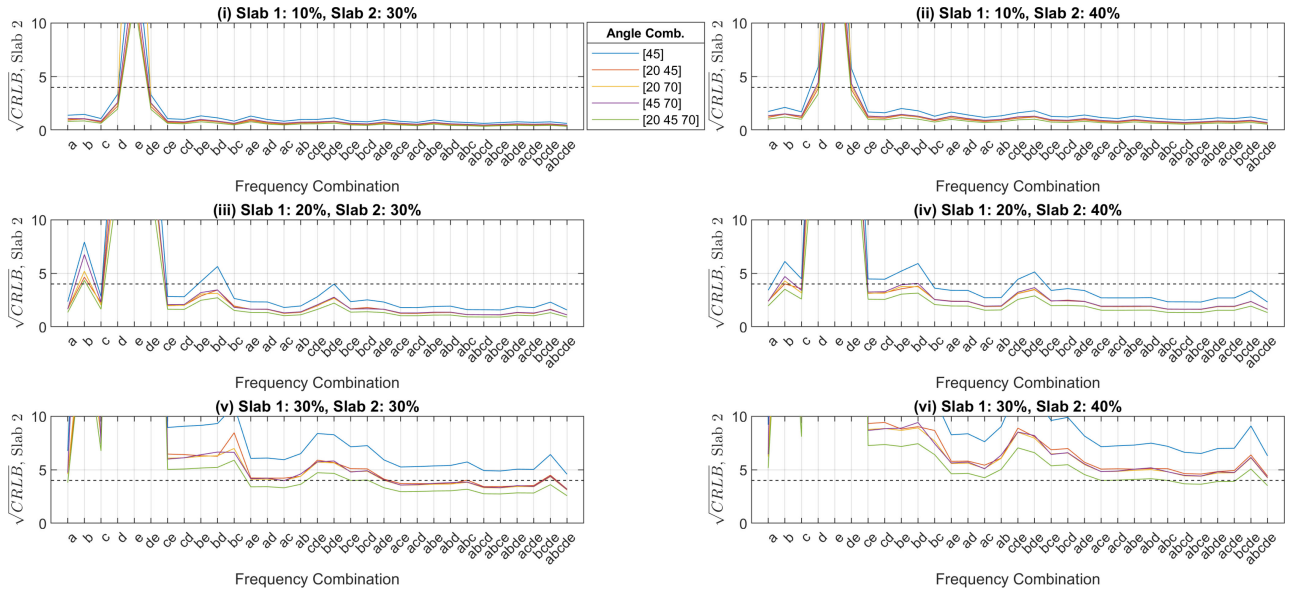


Fig. 5. Root-zone soil moisture  $\sqrt{\text{CRLB}}$  as a function of frequency. Frequency combinations are noted along the  $x$ -axis where  $a, b, c, d,$  and  $e$  correspond to 137, 255, 370, 1575, and 2338 MHz, respectively. The second slab is fixed at 30 cm below the air–surface boundary. The colored lines show combinations of incidence angle measurements corresponding to the legend at the top of the figure.

are resolved. Thus, the reduced sensitivity at certain angles is a combination of frequency-dependent and SM profile-dependent properties.

The impact of using different frequency combinations and different incidence angle combinations are shown in Fig. 5 across multiple SM profile configurations. The incidence angles used are  $20^\circ$ ,  $45^\circ$ , and  $70^\circ$ , and the frequency values and notation are the same as those used in (3). As performed previously, each measurement uses all combinations of available frequency, polarization, and incidence angle values. The polarization values used are  $X$  and  $Y$ .

Whenever the SM content, primarily the surface SM, is drier, the use of multiple incidence angles is limited. The benefit of using multiple angles, as well as multiple frequencies, is tied most directly to the surface SM content. As higher surface SM causes more reflections at the surface (and, therefore, less energy traveling toward the second slab), the use of multiple measurements becomes more important. As the surface SM increases, the improvement seen by using multiple incidence angles is also shown to be highly important. Thus, Fig. 5 shows the benefit of using multiple incidence angles as SM content within the profile increases.

While previous simulations have shown that the combination of the lowest frequencies tends to produce the most efficient estimator, the lower-left-most subplot of Fig. 5 shows that the combination  $ab$  (137 and 255 MHz) does not perform as well as all other combinations of 137 MHz with another frequency. This is reaffirmed by the lower-left subplot of Fig. 2 where 255 MHz is shown to be an unideal estimator for a slab fixed at 30 cm in the SM profile. This stresses the importance of frequency-, depth-, and SM-dependent interactions in the  $\sqrt{\text{CRLB}}$  calculation.

Because incidence angle alters the amount of energy transmitted into the SM profile, it can be thought of as adjusting one's sensitivity to the depth of the profile. For this reason,

multiple combinations allowing one to have adjusted sensitivity to the profile, allowing for better estimation at different depths. This property justifies the improved  $\sqrt{\text{CRLB}}$  with respect to increasing number of incidence angles as shown in Fig. 5.

2) *Varying Polarization*: The effects of combining four polarization states of the receiver are shown in Fig. 6. Within the upper-left and upper-right subplots, all five frequencies are used, and angles of  $20^\circ$ ,  $45^\circ$ , and  $70^\circ$  incidence are used. Within the lower-left and lower-right subplots, the effect of reducing measurements to a pairing of 137 and 255 MHz (shown in the solid line) and the pairing of 370 and 1575.42 MHz frequencies (shown in the dashed line) is depicted. The  $x$ -axis indicates the polarization of the receiver and the number of combinations used for a maximum of two polarizations across  $X, Y, R,$  and  $L$  polarizations.

Since the wave of a specular, incident signal on the air–surface boundary tends to induce a  $90^\circ$  phase shift and change the polarization state,  $\sqrt{\text{CRLB}}$  values that only use  $R$  polarization do not provide much benefit for the calculation of the  $\sqrt{\text{CRLB}}$  at  $20^\circ$  incidence. However, the remaining  $L, X,$  and  $Y$  information provides significant benefit, especially at higher SM conditions. Unlike Figs. 4 and 5, where the resulting  $\sqrt{\text{CRLB}}$  changed depending on the SM profile, the  $\sqrt{\text{CRLB}}$  here seems to only be scaled as the SM profile varies. When the number of frequencies is reduced, we observe the same trend in the changing  $\sqrt{\text{CRLB}}$  as a function of polarization but with a higher  $\sqrt{\text{CRLB}}$  value caused by eliminating important information from the CRLB calculation. Ultimately, the effect of polarization appears to be relatively independent of frequency as each line shown observes the same shape at different amplitudes as controlled by the polarization information. In general, the use of the cross-polarized signal ( $L$ -polarization for these simulations) provides the most information. Additional polarization information, however, can be useful in estimation of more wet soils as shown in



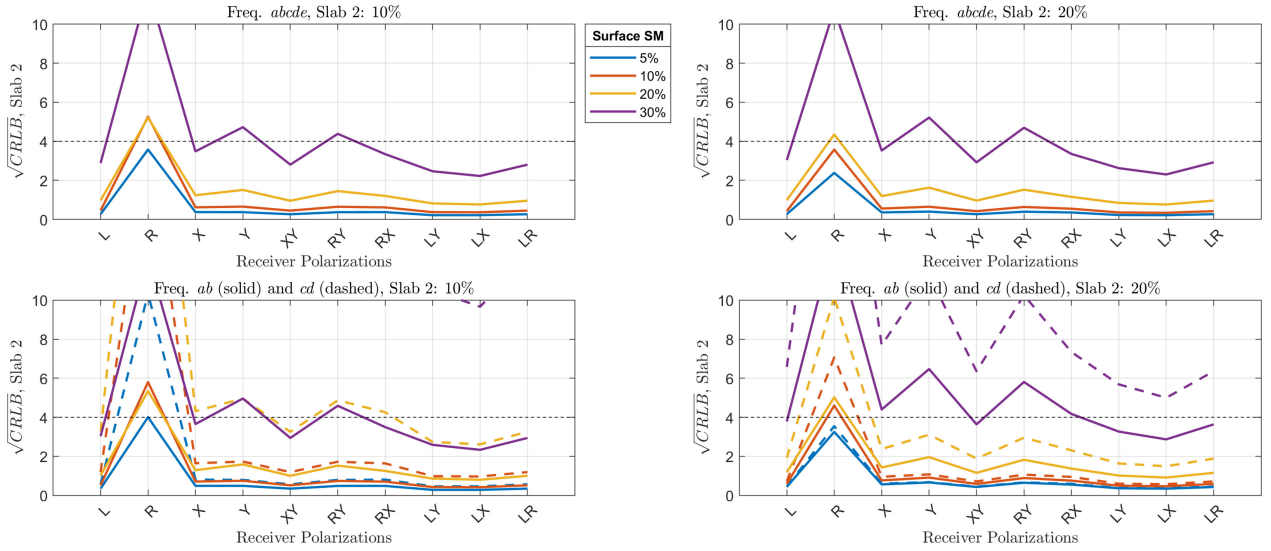


Fig. 6. Root-zone soil moisture  $\sqrt{\text{CRLB}}$  as a function of polarization. Each measurement uses incidence angles of  $20^\circ$ ,  $45^\circ$ , and  $70^\circ$ . The top row uses all available frequencies (137, 255, 370, 1575.42 and 2338 MHz) denoted by the letters *abcde*. The bottom row depicts two separate dual frequency combinations. The combination represented by the solid line uses 137 and 255 MHz as denoted by the letters *ab*. Dashed lines use 370 and 1575.42 MHz as denoted by the letters *cd*. The *x*-axis value represents the receiver's polarization measurement used by each frequency and incidence angle measurement.

the lower-right subplot for the line representing 30% surface SM.

While there is clearly increased performance when the RZSM value increases from 10% to 20%, this behavior is caused by the interaction of the signals with the provided multilayer dielectric structure. This SM-profile-specific behavior is illustrated most clearly in the following section.

### C. CRLB as a Function of Soil Moisture

For this simulation, the  $\sqrt{\text{CRLB}}$  as a function of surface SM and RZSM is visualized for selected SoOp-R configurations. Fig. 7 depicts the second slabs  $\sqrt{\text{CRLB}}$  of a two-slab configuration at 30 cm under varying SM conditions. The upper and lower SM slabs are swept across SM from 5% to 50% in 1% increments. Six receiver configurations are depicted. Each subplot in the left column uses information provided by *X*- and *Y*-polarized signals as well as three angles ( $20^\circ$ ,  $45^\circ$ , and  $70^\circ$ ). Each subplot in the right column uses information provided by *L*-polarized signals at  $20^\circ$  incidence only. The top row of subplots uses all five frequencies, the middle row of subplots uses two frequencies (370 and 1575 MHz), and the bottom row of subplots uses two frequencies (137 and 255 MHz). The number of total measurements is depicted in the title of each subplot. Thus, the total number of measurements range from 5 to 30 for the top row of subplots, and the two remaining rows range from 2 to 12 measurements.

These simulations most clearly show the relationship between the number of measurements, SM, and frequency for calculating the  $\sqrt{\text{CRLB}}$  of RZSM at 30 cm. The upper-left simulation using the most observations shows an ideal case where 30 measurements are taken at many frequencies. For this measurement configuration, the  $\pm 4\%$   $\sqrt{\text{CRLB}}$  is achieved across a range of surface and root-zone SM combinations where (35, 15)% and

(26, 50)% serve as the two endpoints achieving this desired threshold. This subplot also shows that the  $\sqrt{\text{CRLB}}$  at 30 cm will achieve, at its worst, a 5% error for any combination of SM values for the provided range.

By reducing the number of measurements from 30 to 5 as shown in the upper-right subplot, we can visualize the effect of using fewer measurements with multiple frequencies. By comparing the upper-left subplot and the upper-right subplot, it can be seen that the  $\sqrt{\text{CRLB}}$  values all shift downward along the RZSM axis and to the left on the surface SM axis. After accounting for this shift, the shape of the image representing the CRLB values at each location is generally maintained. In other words, the use of multiple frequencies is able to perform similar estimation at the tradeoff of lower SM values overall. The endpoints of the curve achieving a 4%  $\sqrt{\text{CRLB}}$  with surface SM and RZSM values is (30, 5)% and (20, 50)%.

The mid-left and lower-left subplot visualizes the impact on the  $\sqrt{\text{CRLB}}$  by using only 2 frequencies with a total of 12 measurements from combinations of polarization and incidence angle. When the upper-left subplot of 30 observations from 5 frequencies is used as reference, the shape of the  $\sqrt{\text{CRLB}}$  image is shown to change significantly. Where the two upper subplots visualize a point where all succeeding surface SM values yield a  $\sqrt{\text{CRLB}}$  beyond 10%, the color red two images here create a sort of blind-spot between surface SM values where the  $\sqrt{\text{CRLB}}$  increases significantly before decreasing again at a higher SM value (e.g., between 25% and 35% surface SM in the lower-left subplot.) This is caused directly by the sensitivity of the frequencies used to calculate the  $\sqrt{\text{CRLB}}$ . Thus, increasing the number of frequency sources has the effect of smoothing out the blind-spots for SM combinations in the profile. This simulation reconfirms the frequency-dependent behavior observed in Fig. 3. Generally, however, the endpoints of surface and root-zone SM values achieving a 4%  $\sqrt{\text{CRLB}}$  are (35, 15)% and (32, 38)%

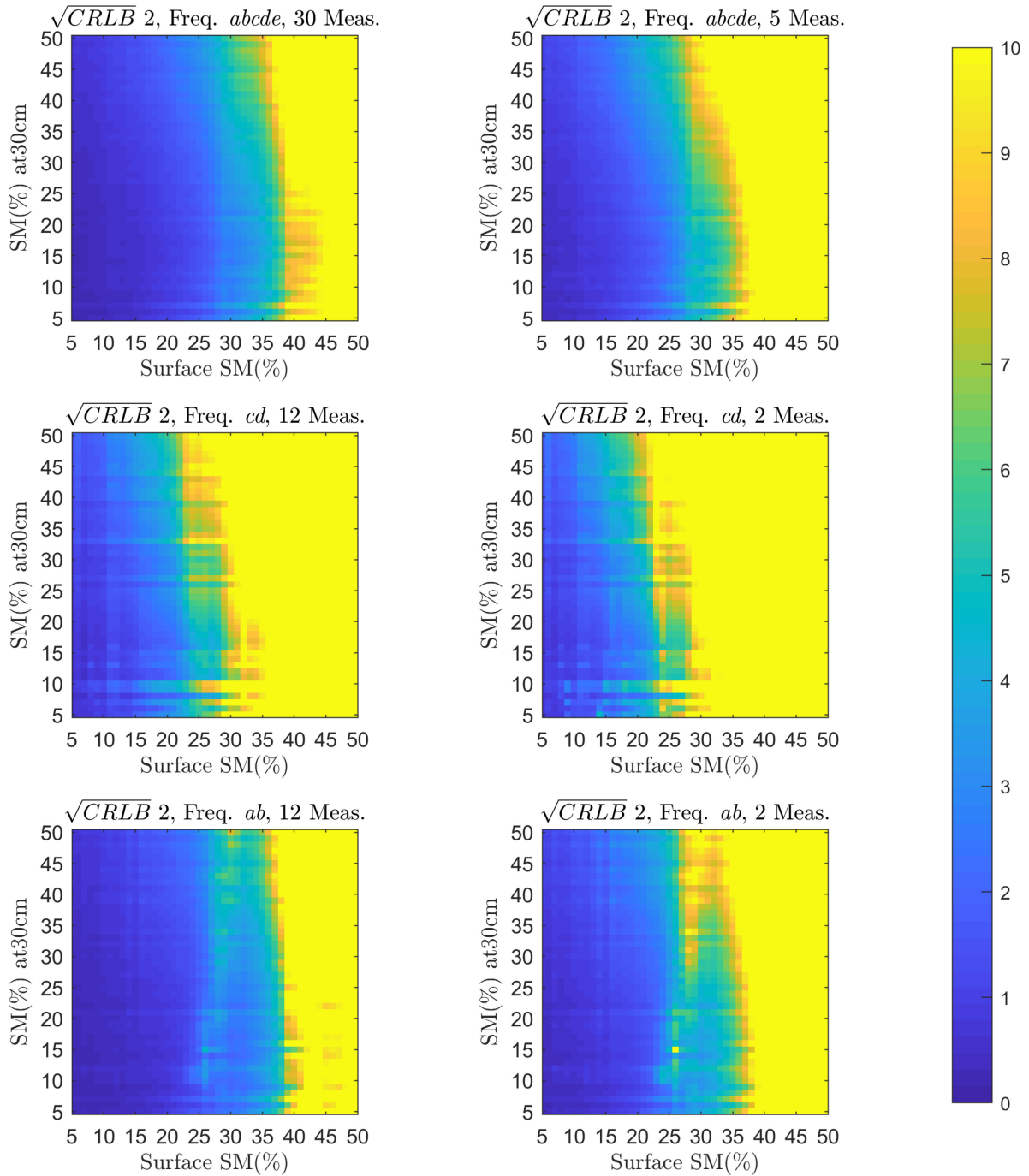


Fig. 7. Root-zone soil moisture  $\sqrt{CRLB}$  as a function of surface and root-zone soil moisture. All subplots in the left column use X and Y polarizations and three angles (20°, 45°, and 70°). All subplots in the right column use L polarization and a 20° angle. The top row uses all available frequencies (137, 255, 370, 1575.42, and 2338 MHz) denoted by the letters *abcde*. The middle row uses two frequencies (137 and 255 MHz) denoted by the letters *ab*. The bottom row uses two frequencies (370 and 1575 MHz) denoted by the letters *cd*. The title of each subplot denotes the number of measurements used in each configuration.

for the mid-left subplot and are (28, 15)% and (18, 50)% for the lower-left subplot.

The mid-right and lower-right subplots show the effects of reducing the 12 measurements from the mid- and lower-left subplot down to 2. When this occurs, the endpoints achieving a 4%  $\sqrt{CRLB}$  are (34, 9)% and (21, 50)% for the mid-right subplots and (24, 5)% and (12, 50)% for the mid-lower-right

subplots. The general shape of the mid- and lower-left subplot is maintained, but the reduced number of measurements from polarization and incidence angle make the limit the desired  $\sqrt{CRLB}$  to shallower depths.

Overall, it is observed that reducing frequencies produces a more varied error  $\sqrt{CRLB}$ . When either polarization observations or incidence angle measurements are reduced, the

maximum RZSM value corresponding to the calculated  $\sqrt{\text{CRLB}}$  threshold is also reduced. However, the overall shape of the image is maintained.

This simulation also visualizes how the  $\sqrt{\text{CRLB}}$  calculation is specific to frequency-dependent interactions with the multi-layered SM profile structure. As shown in the middle and lower subplots, large patches in the SM/RZSM values where one might expect a linear change in the  $\sqrt{\text{CRLB}}$  result in large fluctuations. Even without such large changes, each subplot shows small fluctuations in the  $\sqrt{\text{CRLB}}$  where the value either increases or decreases in somewhat unexpected ways. This behavior was previously displayed in Fig. 6 when the  $\sqrt{\text{CRLB}}$  value decreased despite the RZSM value increasing. This behavior is caused by the sensitivity of the different wavelengths to changes in the profile's dielectric. It can be reasonably assumed that, given a sufficient number of frequency sources, these unexpected fluctuations in  $\sqrt{\text{CRLB}}$  can be eliminated.

#### IV. DISCUSSION

The results of this article assist in visualizing the range of potential inversion accuracy for a wide variety of SM configurations and SoOp-R configuration scenarios. In order to mirror the common target 4% estimation accuracy of SM seen across multiple SM-centric remote sensing missions, this article primarily focuses on analyzing where a 4%  $\sqrt{\text{CRLB}}$  value is achieved. The range at which this is achievable is highly dependent on the RZSM depth, the SM content of the profile, and the SoOp-R configuration. The results suggest that if one were to follow this modeling pursuit of a two-layer dielectric slab, an RZSM data product should potentially include an indication of the location in the profile where the SM is being sensed due to the sensing depth being highly variable. The simulations shown provide a framework which can potentially aid in SoOp-R receiver design for characterizing system performance at varying ground and receiver-system conditions.

This article works under the assumption that the SoOp-R measurements experience complex Gaussian noise. While there is precedent in the literature for assuming that the noise for such a SoOp-R-based SM measurement is Gaussian [32], this may not be the case for all circumstances. Different scattering surfaces could potentially induce different noise distributions which would require different assumptions for CRLB studies.

The same noise variance is used for each frequency in this article. It is unlikely that the noise variance for each system will be identical in reality as the different frequencies/transmitter systems will have independent features that will affect the SNR of the SoOp-R system. For example, different coherent integration times could easily change the total SNR for the system. At this time, the authors are unaware of any noise characterization that has been performed on these systems for SoOp-R applications. While this article helps to establish the general impact that multiple parameters have on the estimation accuracy, noise variances tailored to each system will help characterize future studies more accurately for the currently available communication systems.

While incidence angle alters the available energy incident upon the surface, incidence angle does not significantly affect the

SoOp-R measurement. Because of this, there does not appear to be any incidence angle which provides a more optimal solution if results are contained in a region that does not approach grazing angle. Similarly, the benefit of multipolarization measurements for RZSM estimation is largely from the addition of observed measurements. Assuming that the polarization is not copolarized relative to a circularly polarized transmitter, any standard polarization choice will produce comparable results for lower SM values. As the SM content increases, the differences will become more pronounced. For a circularly polarized source, the optimal antenna in terms of obtaining the minimum  $\sqrt{\text{CRLB}}$  will use cross-polarization.

A critical assumption made by this article is that two discrete values representing SM and RZSM are unknown parameters to be solved simultaneously. However, there are many representations and approaches which can be used to solve for RZSM. For example, by fixing the surface SM value based on available data products from resources such as soil moisture active passive (SMAP) and soil moisture ocean salinity (SMOS) missions, the CRLB can assuredly be further improved. Alternatively, many inversion-based RZSM papers assume that SM is represented by several discrete layers in the profile (as opposed to the two used here) which can be parameterized by SM mapping functions. The decision by this article to use two slabs was chosen, in part, to easily visualize the joint effects of known and unknown parameters on estimation accuracy. Further research can explore the impact of discretization of the SM profile on the CRLB, but this is beyond the scope of this article.

Surface roughness is a critical variable that not only decreases the reflection coefficient, but it also contributes to non-negligible incoherent scattering once the roughness exceeds the Rayleigh scattering criterion. In particular, the compounding effects of surface roughness and topography could be significant over contributing areas within a spaceborne receivers footprint while will generally be on the order of several hundreds of meters. While previous research has observed successful surface SM estimation from GNSS-R signals under a dominantly coherent signal assumption [33]–[35], the effects of topography and surface roughness deserve an in-depth analysis for these spatial scales [36]–[38]. Under a moderately smooth surface assumption ( $\approx 1.5$  cm), coherent signals at L-band and lower will be minimally effected by surface roughness. However, S-band signals will likely be dominantly incoherent at such scales. The joint usage of coherent and incoherent signals should be explored for a variety of topographies and surface roughness values to understand how these components can be leveraged for geophysical parameter estimation from spaceborne platforms.

#### V. SUMMARY AND CONCLUSION

This research presents the study of the  $\sqrt{\text{CRLB}}$  for SM within a two-layer SM profile by means of SoOp-R measurements. The profiles and measurements are created using the open-source modeling and simulation package SCoBi. Within this study, 30 cm is established as a reasonable depth for RZSM estimation. This study investigates the use of the SoOp-R parameters frequency, polarization, and incidence angle for simultaneous

estimation of surface SM ( $\beta_1$ ) and RZSM ( $\beta_2$ ). These parameters are used because engineers possess some degree of control in the design process of a SoOp receiver system.

The depth at which RZSM can achieve a  $\sqrt{\text{CRLB}}$  of 4% is examined by observing the  $\sqrt{\text{CRLB}}$  as a function of depth for multiple SM profile configurations and two SoOp-R configurations. The two SoOp-R configurations both use 5 frequencies where the first configuration uses 120 measurements from a combination of 6 angles and 4 polarization measurements, while the second is restricted to observations at  $L$ -polarization and  $20^\circ$  incidence. The 4% lower bound is achieved at 45 cm for the configuration using 120 measurements and 27 cm for a configuration using 5 measurements for a SM profile composed of 30% surface SM and 10% RZSM.

The combined effects of frequency and depth are visualized in Fig. 3. The results show that an estimator using a single frequency which achieves low  $\sqrt{\text{CRLB}}$  values may exist. However, changes in the slab position and SM content will consistently cause sharp changes in  $\sqrt{\text{CRLB}}$  at potentially unforeseeable depths due to nature of SoOp-R interaction with the profile. The addition of a single frequency will largely eliminate these abrupt changes in  $\sqrt{\text{CRLB}}$ . Longer wavelengths are seen to be the most significant factor in increasing the depth at which RZSM can be estimated as one would expect. Based on the problem configuration, this article chooses to examine the effects that polarization, incidence angle, and SM content play on the  $\sqrt{\text{CRLB}}$  for RZSM content at 30 cm as this depth provides reasonable estimation above the noise floor for this system.

For polarization and incidence angle measurements, it is found that both variables are helpful in estimating moderately wet SM content. As for polarization, the  $\sqrt{\text{CRLB}}$  is calculated from a combination of five frequencies and three angle measurements ( $20^\circ$ ,  $45^\circ$ , and  $70^\circ$ ) as well as at two frequencies (both pairings of 137 and 255 MHz as well as 370 and 1575.42 MHz) with the same angle measurements. It is observed that polarization observations largely perform the same assuming that the receiver is not copolarized with respect to a circularly polarized transmitter. However, increasing the number of polarizations used does improve the  $\sqrt{\text{CRLB}}$  moderately. For incidence angles, it is found that incidence angles between  $0^\circ$  and  $75^\circ$  ensure stable  $\sqrt{\text{CRLB}}$  when all five frequencies are used. When the frequencies are reduced, some frequency-dependent uncertainties can occur with respect to incidence based on the wavelengths interaction with different SM profile configurations at different angles.

A sweep for multiple SM profile configurations is examined under different SoOp-R configurations. It is found that RZSM at 30 cm can achieve a  $\sqrt{\text{CRLB}}$  of 4% with as few as two measurements, given sufficient SM profile configurations. When the number of frequencies is limited, the 4% threshold between surface SM and RZSM borders will become increasingly non-linear; however, this border is made more linear with increasing frequency combinations. RZSM with a  $\sqrt{\text{CRLB}}$  of 4% can be estimated when both surface SM and RZSM are 30%, given 30 measurements. If only two frequencies are used, RZSM can be estimated with 4%  $\sqrt{\text{CRLB}}$  if surface SM and RZSM are limited

to 20% for a combination of 370 and 1575 MHz while a pairing of 137 and 255 MHz can achieve this  $\sqrt{\text{CRLB}}$  at 30% surface SM.

## REFERENCES

- [1] S. Gleason, "Remote sensing of ocean, ice and land surfaces using bistatically scattered GNSS signals from low earth orbit," Ph.D. dissertation, Univ. Surrey, Guildford, England, 2006.
- [2] C. S. Ruf *et al.*, "The CYGNSS nanosatellite constellation hurricane mission," in *Proc. Int. Geosci. Remote Sens. Symp.*, Jul. 2012, pp. 214–216.
- [3] V. U. Zavorotny, S. Gleason, E. Cardellach, and A. Camps, "Tutorial on remote sensing using GNSS bistatic radar of opportunity," *IEEE Geosci. Remote Sens. Mag.*, vol. 2, no. 4, pp. 8–45, Dec. 2014.
- [4] J. L. Garrison, S. J. Katzberg, and C. T. Howell, "Detection of ocean reflected GPS signals: Theory and experiment," in *Proc. IEEE SoutheastCon*, 1997, pp. 290–294.
- [5] M. Martín-Neira, S. D'Addio, C. Buck, N. Floury, and R. Prieto-Cerdeira, "The PARIS ocean altimeter in-orbit demonstrator," *IEEE Trans. Geosci. Remote Sens.*, vol. 49, no. 6, pp. 2209–2237, Jun. 2011.
- [6] J. Tye, P. Jales, M. Unwin, and C. Underwood, "The first application of stare processing to retrieve mean square slope using the SGR-ReSI GNSS-R experiment on TDS-1," *IEEE J. Sel. Top. Appl. Earth Obs. Remote Sens.*, vol. 9, no. 10, pp. 4669–4677, Oct. 2016.
- [7] C. C. Chew, E. E. Small, K. M. Larson, and V. U. Zavorotny, "Effects of near-surface soil moisture on GPS SNR data: Development of a retrieval algorithm for soil moisture," *IEEE Trans. Geosci. Remote Sens.*, vol. 52, no. 1, pp. 537–543, Jan. 2014.
- [8] N. Pierdicca, L. Guerriero, A. Egido, S. Paloscia, and N. Floury, "Exploiting GNSS signals for soil moisture and vegetation biomass retrieval," in *Proc. IEEE Int. Geosci. Remote Sens. Symp.*, 2015, pp. 5119–5122.
- [9] A. Komanduru, "Remote sensing of snow using bistatic radar reflectometry," Open Access Theses, Purdue University, West Lafayette, Indiana, 2016.
- [10] J. Knuble *et al.*, "Airborne P-band signal of opportunity (SoOP) demonstrator instrument; Status update," in *Proc. IEEE Int. Geosci. Remote Sens. Symp.*, 2016, pp. 5638–5641.
- [11] C. C. Chew and E. E. Small, "Soil moisture sensing using spaceborne GNSS reflections: Comparison of CYGNSS reflectivity to SMAP soil moisture," *Geophys. Res. Lett.*, vol. 45, no. 9, pp. 4049–4057, 2018.
- [12] S. Yueh, R. Shah, X. Xu, K. Elder, and B. Starr, "Experimental demonstration of soil moisture remote sensing using P-band satellite signals of opportunity," *IEEE Geosci. Remote Sens. Lett.*, vol. 17, no. 2, pp. 207–211, Feb. 2020.
- [13] J. L. Garrison, J. Piepmeier, R. Shah, M. A. Vega, and D. A. Spencer, "SNOOP: A technology validation mission for P-band reflectometry using signals of opportunity," in *Proc. IEEE Int. Geosci. Remote Sens. Symp.*, 2019, pp. 5082–5085.
- [14] E. Babaeian, M. Sadeghi, S. B. Jones, C. Montzka, H. Vereecken, and M. Tuller, *Ground, Proximal, and Satellite Remote Sensing of Soil Moisture*, 2019. [Online]. Available: <https://doi.org/10.1029/2018RG000618>
- [15] "Board and space studies and national academies of sciences, engineering, and medicine," in *Thriving on Our Changing Planet*. Washington, DC, USA: National Academies Press, Dec. 2018. [Online]. Available: [https://books.google.com/books?hl=en&lr=&id=dumADwAAQBAJ&oi=fnd&pg=PR1&dq=thriving+on+our+changing+planet+&ots=f7A3n\\_j\\_KX&sig=O6AQ-yBZ68TO9NZngjWlZQ5qBOK#v=onepage&q=thriving%20on%20our%20changing%20planet&f=false](https://books.google.com/books?hl=en&lr=&id=dumADwAAQBAJ&oi=fnd&pg=PR1&dq=thriving+on+our+changing+planet+&ots=f7A3n_j_KX&sig=O6AQ-yBZ68TO9NZngjWlZQ5qBOK#v=onepage&q=thriving%20on%20our%20changing%20planet&f=false)
- [16] F. T. Ulaby, "Radar measurement of soil moisture content," *IEEE Trans. Antennas Propag.*, vol. 22, no. 2, pp. 257–265, Mar. 1974.
- [17] E. Chapin *et al.*, "AirMOSS: An airborne P-band SAR to measure root-zone soil moisture," in *Proc. IEEE Natl. Radar Conf.*, 2012, pp. 0693–0698.
- [18] A. Tabatabaenejad, M. Burgin, X. Duan, and M. Moghaddam, "P-band radar retrieval of subsurface soil moisture profile as a second-order polynomial: First AirMOSS results," *IEEE Trans. Geosci. Remote Sens.*, vol. 53, no. 2, pp. 645–658, Feb. 2015.
- [19] A. G. Konings, D. Entekhabi, M. Moghaddam, and S. S. Saatchi, "The effect of a variable soil moisture profile on P-band backscatter estimation," *IEEE Trans. Geosci. Remote Sens.*, vol. 52, no. 10, pp. 6315–6325, Oct. 2014.

- [20] D. R. Boyd *et al.*, "SCoBi multilayer: A signals of opportunity reflectometry model for multilayer dielectric reflections," *Remote Sens.*, to be published.
- [21] S. M. Kay, *Fundamentals of Statistical Signal Processing: Estimation Theory*. Upper Saddle River, NJ, USA: Prentice Hall PTR, 1993.
- [22] N. Pierdicca, L. Pulvirenti, F. Ticconi, and M. Brogioni, "Radar bistatic configurations for soil moisture retrieval: A simulation study," *IEEE Trans. Geosci. Remote Sens.*, vol. 46, no. 10, pp. 3252–3264, Oct. 2008.
- [23] M. A. Ribot, C. Botteron, and P. A. Farine, "Derivation of the Cramér-Rao bound in the GNSS-reflectometry context for static, ground-based receivers in scenarios with coherent reflection," *Sensors*, vol. 16, no. 12, pp. 18–25, 2016.
- [24] D. Comite and N. Pierdicca, "Bistatic radar systems at large baselines for ocean observation," *IEEE Trans. Geosci. Remote Sens.*, vol. 56, no. 3, pp. 1816–1828, Mar. 2018.
- [25] M. Kurum, M. Deshpande, A. T. Joseph, P. E. O'Neill, R. H. Lang, and O. Eroglu, "SCoBi-Veg: A generalized bistatic scattering model of reflectometry from vegetation for signals of opportunity applications," *IEEE Trans. Geosci. Remote Sens.*, vol. 57, no. 2, pp. 1049–1068, Feb. 2019.
- [26] O. Eroglu, D. R. Boyd, and M. Kurum, "SCoBi: A free, open-source, SoOp coherent bistatic scattering simulator framework," in *Proc. IEEE Geosci. Remote Sens. Symp.*, 2018, pp. 1–12.
- [27] O. Eroglu, M. Kurum, and J. Ball, "Response of GNSS-R on dynamic vegetated terrain conditions," *IEEE J. Sel. Top. Appl. Earth Obs. Remote Sens.*, vol. 12, no. 5, pp. 1599–1611, May 2019. [Online]. Available: <https://ieeexplore.ieee.org/document/8719001/>
- [28] V. L. Mironov and S. V. Fomin, "Temperature dependable microwave dielectric model for moist soils," *PIERS Online*, vol. 5, no. 5, pp. 411–415, 2009.
- [29] W. M. Steedly and R. L. Moses, "The Cramer-Rao bound for pole and amplitude coefficient estimates of damped exponential signals in noise," *IEEE Trans. Signal Process.*, vol. 41, no. 3, pp. 1305–1318, Mar. 1993.
- [30] A. J. Kerr, "Theoretical performance bounds for the estimation of target parameters from electromagnetic induction data," Ph.D. dissertation, Georgia Institute Technol., Atlanta, GA, USA, 2020.
- [31] O. Eroglu, M. Kurum, D. Boyd, and A. C. Gurbuz, "High spatio-temporal resolution CYGNSS soil moisture estimates using artificial neural networks," *Remote Sens.*, vol. 11, no. 19, 2019, Art. no. 2272.
- [32] S. H. Yueh, X. Xu, R. Shah, S. Margulis, and K. Elder, "P-Band signals of opportunity for remote sensing of root zone soil moisture," in *Proc. 2018 IEEE Int. Geosci. Remote Sens. Symp.*, pp. 1403–1406, Jul. 2018. [Online]. Available: <https://ieeexplore.ieee.org/document/8518079/>
- [33] V. Senyurek, F. Lei, D. Boyd, M. Kurum, A. C. Gurbuz, and R. Moorhead, "Machine learning-based CYGNSS soil moisture estimates over ISMN sites in conus," *Remote Sens.*, vol. 12, no. 7, 2020, Art. no. 1168.
- [34] C. Chew and E. Small, "Description of the UCAR/CU soil moisture product," *Remote Sens.*, vol. 12, no. 10, 2020, Art. no. 1558.
- [35] Q. Yan, W. Huang, S. Jin, and Y. Jia, "Pan-tropical soil moisture mapping based on a three-layer model from CYGNSS GNSS-R data," *Remote Sens. Environ.*, vol. 247, 2020, Art. no. 111944.
- [36] W. Gu, H. Xu, and L. Tsang, "A numerical kirchhoff simulator for GNSS-R land applications," *Prog. Electromagn. Res.*, vol. 164, pp. 119–133, 2019.
- [37] D. Comite, F. Ticconi, L. Dente, L. Guerriero, and N. Pierdicca, "Bistatic coherent scattering from rough soils with application to GNSS reflectometry," *IEEE Trans. Geosci. Remote Sens.*, vol. 58, no. 1, pp. 612–625, Jan. 2020.
- [38] L. Dente, L. Guerriero, D. Comite, and N. Pierdicca, "Space-borne GNSS-R signal over a complex topography: Modeling and validation," *IEEE J. Sel. Topics Appl. Earth Observ. Remote Sens.*, vol. 13, pp. 1218–1233, Mar. 16, 2020.



**Dylan Ray Boyd** (Member, IEEE) received the B.S. degree in electrical and computer engineering from Mississippi State University (MSU), Mississippi State, MS, USA, in 2017. He is currently working toward the Ph.D. degree in electrical and computer engineering at Electrical and Computer Engineering Department, MSU, where he is continuing his research.

His research focuses on the forward and inverse modeling of SoOp-R scenarios in order to investigate the relationship between SoOp-R and earth science

parameters for remote sensing.



**Ali Cafer Gurbuz** (Senior Member, IEEE) received the B.S. degree in electrical engineering from Bilkent University, Ankara, Turkey, in 2003, and the M.S. and Ph.D. degrees in electrical and computer engineering from Georgia Institute of Technology, Atlanta, GA, USA, in 2005 and 2008.

From 2003 to 2009, he researched compressive sensing-based computational imaging problems at Georgia Tech, Atlanta, GA, USA. He held faculty positions at TOBB University, Ankara, Turkey, and University of Alabama, Tuscaloosa, Alabama, between 2009 and 2017, where he pursued an active research program on the development of sparse signal representations, compressive sensing theory and applications, radar and sensor array signal processing, and machine learning. Currently, he is an Assistant Professor with Department of Electrical and Computer Engineering, Mississippi State University, Mississippi State, MS, USA, where he is Codirector of Information Processing and Sensing (IMPRESS) Lab.

Dr. Gurbuz is a member of Sigma Xi. He is the recipient of The Best Paper Award for Signal Processing Journal, in 2013 and the Turkish Academy of Sciences Best Young Scholar Award in Electrical Engineering, in 2014. He has served as an Associate Editor for several journals such as *Digital Signal Processing*, *EURASIP Journal on Advances in Signal Processing*, and *Physical Communications*.



**Mehmet Kurum** (Senior Member, IEEE) received the B.S. degree in electrical and electronics engineering from Bogazici University, Istanbul, Turkey, in 2003, and the M.S. and Ph.D. degrees in electrical engineering from George Washington University, Washington, DC, USA, in 2005 and 2009, respectively.

He held a Postdoctoral position with the Hydrological Sciences Laboratory, NASA Goddard Space Flight Center, Greenbelt, MD, USA. In 2016, he was an Assistant Professor with the Department of Electrical and Computer Engineering, Mississippi State University, Mississippi State, MS, USA. His research interests include microwave and millimeter-wave remote sensing, RF sensors and systems, radiation and scattering theory, and signals of opportunity.

Dr. Kurum is an Early Career Representative for the International URSI Commission F (Wave Propagation and Remote Sensing). He was a recipient of the Leopold B. Felsen Award for excellence in electromagnetic, in 2013 and the International Union of Radio Science (URSI) Young Scientist Award, in 2014.



**James L. Garrison** received the B.S. degree from the Rensselaer Polytechnic Institute, Troy, NY, USA, the M.S. degree from Stanford University, Stanford, CA, USA, and the Ph.D. degree from the University of Colorado Boulder, Boulder, CO, USA, in 1988, 1990, and 1997, respectively.

He is a Professor with the School of Aeronautics and Astronautics, Purdue University, West Lafayette, IN, USA, with a courtesy appointment at the School of Electrical and Computer Engineering. His research interests include earth remote sensing using global

navigation satellite systems (GNSS) and signals of opportunity. He is the Principal Investigator for SNOOPI, a NASA mission to demonstrate remote sensing with P-band signals of opportunity. Prior to his academic position, he was with the National Aeronautics and Space Administration (NASA).

Dr. Garrison is a fellow of the Institute of Navigation (ION) and Editor-in-Chief for the *IEEE Geoscience and Remote Sensing Magazine*.



**Benjamin R. Nold** (Graduate Student Member, IEEE) received the M.S.E.C.E. degree from Purdue University, West Lafayette, IN, USA, in 2019. He is currently working toward the Ph.D. degree in electrical and computer engineering at Purdue University, developing new remote sensing instruments using signal of opportunity for earth remote sensing applications.

He is researching signal processing algorithms for spaceborne SoOp instruments.



**Jeffrey R. Piepmeier** (Senior Member, IEEE) received the B.S. Engineering degree in electrical concentration from LeTourneau University, Longview, TX, USA, in 1993, and the M.S. and Ph.D. degrees in electrical engineering from the Georgia Institute of Technology, Atlanta, GA, USA, in 1994 and 1999, respectively.

He is currently the Chief Passive Microwave Instrument Engineer with the Instrument Systems and Technology Division, NASA Goddard Space Flight Center (GSFC), Greenbelt, MD, USA, and serves as

a Deputy Coordinator for the Aerosols, Clouds, Convection and Precipitation architecture study and as Technology Co-Lead for the Planetary Boundary Layer study team. He is an Instrument Scientist for the SMAP radiometer and GPM Microwave Imager. Previously at GSFC, he was Associate Head of the Microwave Instruments and Technology Branch and Instrument System Engineer for the Aquarius Radiometer. He was Deputy PI on the IceCube CubeSat mission and led the Goddard teams on the CubeRRT and SNOOPI CubeSat missions. Before joining NASA, he was a Student Employee with Vertex Communications Corporation and a Shackleford Fellow with Georgia Tech Research Institute. His research interests include microwave radiometry and technology development to enable the next generation of microwave sensors.

Dr. Piepmeier is a member of URSI (Commission F). He is a past Chairperson of the GRSS Instrumentation and Future Technologies technical subcommittee and past Chairperson of the National Academies' Committee on Radio Frequencies (CORF). He was the recipient of an Excellence in Federal Career Gold Award (Rookie-of-the-year), in 2000 and was a 2002 NASA Earth Science New Investigator. He was the recipient of five NASA Group Achievement Awards, NASA's Exceptional Engineering Achievement Medal for advances in RFI mitigation technology, NASA's Exception Achievement Medal for significant contributions to the Aquarius/SAC-D mission, and NASA's Outstanding Leadership Medal for contributions of Aquarius, GPM, and SMAP.



**Manuel A. Vega** (Member, IEEE) received the B.S. and M.S. degrees in electrical engineering from the University of Puerto Rico, Mayagez, Puerto Rico, and the Ph.D. degree from Colorado State University, Fort Collins, CO, USA.

He is an Engineer with the Microwave Instruments and Technology Branch, NASA Goddard Space Flight Center, Greenbelt, MS, USA. Throughout his career, he has worked on multiple active and passive remote sensing instruments spanning the VHF to IR spectrum in various roles. Applications include airborne P-band signals of opportunity reflectometer and L-band SAR, X-band precipitation radar, Ku/Ka-band airborne and polarimetric ground-based precipitation radars, as well as mm-wave/IR polarimetric conical scanning radiometer for cloud observations. Since 2019, he supports the signals of opportunity P-band Investigation (SNOOPI) as Co-I and Instrument Development Lead.



**Rajat Bindlish** (Senior Member, IEEE) received the B.S. degree in civil engineering from IIT Bombay, Mumbai, India, in 1993, and the M.S. and Ph.D. degrees in civil engineering from Pennsylvania State University, State College, PA, USA, in 1996 and 2000, respectively.

He is currently with NASA Goddard Space Flight Center, Greenbelt, MD, USA. Prior to this, he was with the USDA Agricultural Research Service, Hydrology and Remote Sensing Laboratory, Beltsville, MD, USA. He is currently working on soil moisture estimation from microwave sensors and their subsequent application in land surface hydrology. His research interest involves the application of microwave remote sensing in hydrology.

Dr. Bindlish is a member of the American Geophysical Union. He is also a Science Team Member of SMAP, NISAR, Aquarius, and GCOM-W missions.